

Time scales for pluton growth, magma chamber formation and super-eruptions

Stephen Sparks (✉ steve.sparks@bristol.ac.uk)

Bristol University

Marit van Zalinge

Bristol University

Darren Mark

Scottish Universities Environmental Research Centre

Marissa Tremblay

Purdue University <https://orcid.org/0000-0001-9984-9554>

Brenhin Keller

Dartmouth College

Francis Cooper

University of Bristol

Alison Rust

University of Bristol

Physical Sciences - Article

Keywords: silicic magma, super-eruptions, sanidine crystals

Posted Date: May 25th, 2021

DOI: <https://doi.org/10.21203/rs.3.rs-447477/v1>

License:   This work is licensed under a Creative Commons Attribution 4.0 International License.

[Read Full License](#)

Version of Record: A version of this preprint was published at Nature on August 3rd, 2022. See the published version at <https://doi.org/10.1038/s41586-022-04921-9>.

1 Time scales for pluton growth, magma chamber formation and super-eruptions

2

3 M.E. van Zalinge¹, D.F. Mark^{2,3}, R.S.J. Sparks¹, Tremblay, M.M.⁴, C.B. Keller⁵, F.J. Cooper¹ and

4 A. Rust¹

5

6 1. School of Earth Sciences, University of Bristol, Wills Memorial Building, Bristol BS8 1RJ,
7 United Kingdom.

8 2. Scottish Universities Environmental Research Centre, Rankine Avenue, Scottish
9 Enterprise Technology Park, East Kilbride, G75 0QF, United Kingdom.

10 3. Department of Earth and Environmental Science, University of St Andrews, St
11 Andrews, KY16 9AJ, UK

12 4. Department of Earth, Atmospheric and Planetary Sciences, 550 Stadium Mall Drive,
13 Purdue University, West Lafayette, IN 47907-2051, U.S.A.

14 5. Department of Earth Sciences, Dartmouth College, Hanover, NH 03755, U.S.A.

15

16 **Summary**

17

18 *Generation of silicic magmas leads to emplacement of granite plutons, huge explosive volcanic*
19 *eruptions and physical and chemical zoning of continental and arc crust¹⁻⁷. While the time*
20 *scales for silicic magma generation in the deep and middle crust are prolonged⁸ magma*
21 *transfer into the upper crust followed by eruption is episodic and can be rapid⁹⁻¹². Ages of*
22 *inherited zircons and sanidines from four Miocene ignimbrites in the Central Andes indicate a*
23 *gap of 4.6 Myr between the start of pluton emplacement and onset of super-eruptions, with*
24 *a 1 Myr cyclicity. Here we show that inherited sanidine crystals were stored at temperatures*

25 <470°C prior to incorporation in the magma. Our observations are explained by silicic melt
26 segregation in a middle crustal hot zone with episodic melt ascent from an unstable layer at
27 the top of the zone with a time scale governed by the rheology of the upper crust. After
28 thermal incubation of the growing batholith, large magma chambers formed in only a few
29 thousand years or less by dyke transport from the hot zone melt layer. Instability and
30 disruption of earlier plutonic rock occurred in a few decades or less just prior to or during
31 super-eruptions.

32

33 Large-volume silicic ignimbrites are co-genetic with emplacement of large granitoid
34 batholiths in the upper crust¹⁻⁵. Ignimbrites provide snapshots in the evolution of batholith
35 systems and contain information about pluton emplacement and silicic magma chamber
36 formation from geochronology and crystal residence time studies⁶⁻¹¹, complemented by
37 numerical modelling¹²⁻¹⁷. Upper crustal silicic igneous systems are part of transcrustal
38 magmatic systems in which differentiated (silicic) melts are generated in the middle and lower
39 crust by reactive flow in mushes created by long-term influx of basalt^{8,18-21}. Buoyancy
40 instabilities^{8,22} within transcrustal magmatic systems drive differentiated magmas to shallow
41 crustal levels, sometimes resulting in silicic volcanism.

42

43 The longevity of plutonic and related volcanic systems (typically 10^6 to 10^7 years)^{1-7,17}
44 contrasts with short timescales (typically $< 10^3$ years) to assemble shallow magma chambers
45 prior to large-magnitude ignimbrite eruptions^{9-11,23}. Some crystals (antecrysts) entrained
46 within erupting magmas are stored at temperatures near or even below the solidus for long
47 periods of time prior to eruption²⁴. These observations raise questions about silicic magma

48 generation, plutons emplacement, magma chamber formation and how super-eruptions are
49 triggered.

50

51 We present new $^{40}\text{Ar}/^{39}\text{Ar}$ ages on tens of individual sanidine fragments sampled from early
52 Miocene rhyolitic ignimbrites located in northern Chile. These data are utilised along with
53 $^{206}\text{Pb}/^{238}\text{U}$ single crystal CA-ID-TIMS and laser-ablation ICP-MS zircon geochronology.
54 Terminology for magmatic systems is summarised in methods.

55

56 **Geological background**

57 The Oxaya Formation, located on the western slope of the Central Andes (Figure 1), comprises
58 four large volume (collectively $> 2000 \text{ km}^3$) regional ignimbrites^{25,26}. Their ages are:
59 Poconchile (22.626 \pm 0.0531/-0.060 Ma); Cardones (21.840 \pm 0.048/-0.054 Ma); Molinos
60 (20.821 \pm 0.057/-0.068 Ma) and Oxaya (19.553 \pm 0.049/-0.053 Ma). The ages are 95%
61 confidence interval including systematic uncertainties. Poconchile, Cardones and Oxaya ages
62 were determined by applying a Bayesian model to integrate single-crystal zircon U-Pb ID-TIMS
63 $^{206}\text{Pb}/^{238}\text{U}$ analyses of the youngest crystals identified by LA-ICPMS screening²⁵ and single
64 crystal sanidine $^{40}\text{Ar}/^{39}\text{Ar}$ ages (methods). The ages (Figure 2) are modified from van Zalinge
65 et al.²⁵. The Molinos age is a new $^{40}\text{Ar}/^{39}\text{Ar}$ analysis of sanidine.

66

67 The Oxaya ignimbrites are rhyolites with mineral assemblages of plagioclase, quartz, biotite,
68 FeTi oxides, \pm sanidine and \pm amphibole^{25,27} and ubiquitous accessory zircon. The Cardones
69 ignimbrite²⁶ is crystal-rich (ca 30-40%) and contains two petrologically distinct pumice
70 varieties, one with high sanidine content but no amphibole and the other with low or no
71 sanidine and minor amphibole. Magma temperatures are estimated²⁷ in the range 850-750°C

72 for the sanidine-poor magma and 770-670°C for the sanidine-rich magma. Barometry and
73 thermometry, together with rare earth element data, indicate generation of the silicic
74 magmas by differentiation from wet basaltic to andesitic magmas with temperatures of 950-
75 850°C emplaced in the middle and lower crust at depths of approximately 15 km or more.
76 Isotopic data indicate assimilation of older crust²⁸. The silicic magmas were emplaced into the
77 upper crust at estimated depths from 6.0 to 8.7 ± 2.0 km²⁷.

78

79 **Geochronology of sanidines and inherited zircons**

80 Single-fragment ⁴⁰Ar/³⁹Ar total fusion ages of sanidine and ID-TIMS U-Pb crystallization ages
81 of inherited zircons reveal highly dispersed age spectra for each ignimbrite, with single-crystal
82 ages extending back millions of years prior to eruption (Figure 2). While widely documented
83 in zircon²⁹⁻³¹, age heterogeneity is now being recognized in erupted sanidine^{32,33}. The zircons
84 crystallization ages for Oxaya, Molinos and Cardones extend back millions of years to ages
85 significantly older than apparent ⁴⁰Ar/³⁹Ar ages of sanidines. The time intervals between
86 oldest observed LA-ICPMS spot age and eruption age for each sample are: Cardones (4.2 my);
87 Molinos (3.5 my); and Oxaya (3.5 my).

88

89 The inherited sanidines and zircons indicate a magmatic history extending over 7.7 My
90 between 27.3 Ma and 19.6 Ma for eruption of the youngest ignimbrite. The magma system
91 developed at least 4.6 My prior to the first major ignimbrite. We can exclude significant silicic
92 volcanism in the period 27.3 to 22.7 Ma from observations of lithologies and detrital zircon
93 ages in the late Oligocene to early Miocene Azapa Formation beneath the Oxaya Formation.
94 Volcanic clasts in the Azapa Formation are intermediate³⁴ while only 1 out of 149 detrital
95 zircons³⁵ falls in the 27.3-22.7 Ma period.

96

97 The repose intervals (Figure S2) between the ignimbrite eruptions are calculated as: 0.804
98 +0.065/-0.073 Ma for Poconchile-Cardones; 1.022 +0.078/-0.073 Ma for Cardones-Molinos;
99 and 1.281 +0.074/-0.082 Ma for Molinos-Oxaca. Three ignimbrites (Poconchile, Cardones and
100 Oxaya) indicate continuous zircon crystallization between the oldest age and eruption. Data
101 for Molinos suggest either a hiatus in zircon crystallization over a 1 My period prior to
102 eruption or that the Molinos magma body did not incorporate zircons from this period. The
103 inherited sanidine are qualitatively consistent with the magmatic history implied by the
104 inherited zircons but exhibit a younger and narrower age spread. The percentage of sanidine
105 crystals in each sample that are older than the eruption ages are calculated as: Poconchile
106 (64%); Cardones (60%); Molinos (38%); and Oxaya (45%).

107

108 Inherited sanidines and zircons date back to the early Oligocene (ca. 27 Ma), coinciding with
109 an increase in convergence rate of 6 to 15 cm/year in the period 30 to 25 Ma between the
110 Nazca and South American Plate³⁶. This acceleration is associated with transition from flat
111 slab to steeper subduction³⁶ and onset of large-volume ignimbrite volcanism³⁶⁻³⁹.

112

113 **Interpretation of inherited sanidine data**

114 The ⁴⁰Ar/³⁹Ar ages older than eruption ages may have been modified by mixing or diffusion.
115 Sanidine crystals are commonly zoned²⁷, so the Ar isotopic composition could be a mixture of
116 old crystals and young (eruption age) parts of the crystal resulting in an intermediate age. In
117 between crystallization and eruption, radiogenic ⁴⁰Ar production will be countered by
118 diffusion, which depends exponentially on temperature⁴⁰. We modelled variation of apparent
119 age in sanidine due to diffusive loss of ⁴⁰Ar as a function of crystal size and temperature to

120 constrain storage temperatures. Diffusive loss of ^{40}Ar from sanidine will create rim-to-core
121 age gradients in individual crystals, with the oldest ages preserved in the crystal cores. Our
122 analyses are typically of 0.5 to 1 mm fragments derived from much larger crystals up to 11
123 mm wide, so we calculated the ages of crystal centres.

124

125 Model results (Figure 3a) indicate that ages several Ma older than the eruption age can be
126 preserved in crystal cores if the sanidines are stored at temperatures below $\sim 470^\circ\text{C}$, with the
127 oldest sanidines remaining below 400°C . Previously the concept of cold storage based on
128 zircon geochemistry and geochronology has inferred temperatures at or just below the
129 solidus of rhyolitic magmatic systems ($\sim 700^\circ\text{C}$)²³. Our results show that cold storage can occur
130 at temperatures well below the solidus, as also deduced by Andersen et al.³³ from the
131 presence of old sanidines in the Bishop Tuff.

132

133 Preservation of old ages indicates magma residence times that are very short because
134 diffusion of ^{40}Ar is fast at magmatic temperatures. We calculated the apparent age of sanidine
135 crystal cores as a function of grain size for temperatures of 700°C and 770°C ²⁷, assuming no
136 prior diffusive ^{40}Ar loss during cold storage. The results (Figure 3b) indicate that to preserve
137 the range of observed sanidine ages the residence times must be in the range of years to
138 centuries. For example, for an original grain diameter of 11 mm, ages older than 26 Ma can
139 be preserved in crystal cores for a residence time of ~ 50 years at 700°C or 7-8 years at 770°C .
140 These residence times agree with estimates of annual to decadal timescales for
141 incorporation of inherited crystals into an eruptible magma body and eruption^{8-10,23,24}. Some
142 diffusive loss of ^{40}Ar during cold storage and subsequent residence in the magma can explain
143 why the age range of the zircons extends to greater ages than the sanidines.

144

145 Sanidine crystals may also experience diffusive loss during welding and cooling of ignimbrite.

146 Pumice fiamme were sampled from welded units (Oxaya and Cardones) thick enough to make

147 this a concern. A temperature of 600°C and cooling time of 650 years at 200 m depth were

148 estimated for the Cardones ignimbrite⁴¹. We display calculations of time scales needed to

149 avoid diffusive loss in Figure 3c. For original crystal diameters of 11 mm, ages older than 26

150 Ma can be preserved in the core for $\sim 10^3$ years at 600 °C. Minor losses of ⁴⁰Ar are therefore

151 likely, but are not enough to eradicate the old signatures.

152

153 **Discussion**

154 A conceptual model of magma generation, magma transport and magma chamber formation

155 (Figure 4) builds on emerging ideas of the dynamics and evolution of transcrustal magma

156 systems^{8,19,21}. Here silicic melt generated by reactive flow segregates continuously and slowly

157 within a growing middle crustal hot zone constructed by incremental intrusion of mafic

158 magma²¹. A layer of buoyant silicic melt accumulates at the top of the hot zone. Rayleigh

159 Taylor instabilities develop²² that eventually trigger rapid ascent of large volumes of magma

160 into the upper crust, resulting in granite pluton growth, magma chamber formation and

161 sometimes eruption.

162

163 The Oxaya magmatic system lasted at least 7.7 My, a time comparable to major episodes of

164 batholith intrusion and development of large caldera systems^{1-7,17}. Zircon ages are robust to

165 thermal disturbance, so indicate almost continuous silicic magma generation and

166 crystallization. The magmatic system history involved an initial stage of ~ 4.6 My of pluton

167 growth and a second stage (~ 3.1 My) characterised by episodic large-scale ignimbrite
168 eruptions.

169

170 We interpret the first stage as the incubation period predicted from thermal models of
171 incremental pluton growth^{13-15, 17}. Incubation time is defined as the time for the upper crustal
172 magma reservoir to generate a region with a melt fraction exceeding 0.4¹⁴. During this stage
173 silicic magma is transferred from the middle crust (depths ≥ 15 km) to the upper crust (depths
174 ~ 5 to 8 km)²⁷. From Annen et al.¹⁵ using their equation 7 we estimate an upper limit for
175 magma reservoir growth of 3.5 mm/year over 4.6 My. We envisage pluton growth by
176 displacement of hot ductile crust downwards and sideways¹⁷ (Figure 4). In incremental
177 growth models each increment of magma cools and crystallizes quickly while most of the
178 growing pluton remains at much lower temperature. Models^{13,42} of steady pluton growth
179 indicate that temperatures below 450°C can be sustained across the pluton for growth rates
180 of < 1 cm/year, explaining preservation of old sanidine ages. Lack of silicic volcanic clasts and
181 detrital zircons with early Miocene ages in the underlying Azapa sediments³⁵ suggests that
182 the incubation stage involved only pluton emplacement.

183

184 A persistent magma chamber can develop at the end of the incubation period (Figure 4).
185 However, old sanidine crystals within Oxaya ignimbrites show that magma chamber
186 formation prior to the super-eruptions took place rapidly (decades to centuries) in a very
187 dynamic disruptive environment, indicating highly episodic magma ascent. Episodic
188 emplacement promotes formation of large ephemeral magma chambers^{42,43}.

189

190 We apply a model²² of episodic magma ascent due to Rayleigh Taylor instabilities in slowly
191 developing melt layers at the top of the middle crustal hot zone beneath a subsolidus upper
192 crust with a viscosity μ_c . We propose that repose periods between major ignimbrite are
193 controlled by upper crust rheology. The width of the unstable melt layer, D , determines the
194 wavelength, as it is much less than the unconfined fastest growing wavelength (see methods).
195 The time scale, τ , for an instability to grow into a diapir is (see methods):

196

$$197 \quad \tau = (24\pi\mu_c)/(\Delta\rho g D) \quad (1)$$

198

199 where $\Delta\rho$ is the density contrast ($\sim 300 \text{ kg/m}^3$) between the melt layer and overlying crust.
200 Choosing 1 Myr as the repose period and $D = 40 \text{ km}$ as a typical pluton width we calculate a
201 crustal viscosity of $5 \times 10^{19} \text{ Pa s}$, which is consistent with experimental data⁴³ at 500-700°C.

202

203 We compared dyking and diapirism^{45,46} as mechanisms of magma transport (methods) and
204 conclude only dyke transport is viable to enable rapid formation of upper crustal magma
205 chambers. During RT instability at times comparable to that given by equation 1 conditions
206 for dyke formation at the top of the incipient diapir are inferred to develop. We develop and
207 justify (methods) a simple exchange flow model⁴⁷ of crust with viscosity μ_c slowly subsiding
208 over a large area and magma with viscosity μ_m ascending through a narrow cylindrical conduit
209 as an approximation of dyke transport. Calculations of conduit radii, fluxes, magma chamber
210 volume and assembly time are presented in Table 1 for $\Delta\rho = 300 \text{ kg/m}^3$, $\mu_m = 10^5 \text{ Pa s}$ and μ_c
211 $= 10^{19} \text{ Pa s}$, considering transfer of magma through the conduit from a layer initially 1 km thick
212 of radius R . Three radius values for the collapsing cylindrical crust region are chosen at 15, 20
213 and 25 km to span the scale of large plutons and super-eruption caldera systems. Fluxes are

214 large, explaining how large volume magma chambers can be assembled over periods of a few
215 thousand years.

216

217 Thermal models of episodic pluton growth and magma chamber formation^{13-15,17,42,43} are
218 consistent with the exchange flow model. Episodic magma ascent at rates much higher than
219 time averaged rates are needed to form large upper crustal magma chambers⁴² and are
220 illustrated by parametric models for the Jurassic Yerington batholith in Nevada⁴³. The Luhr
221 Hill pluton has similar geochemical and mineralogical characteristics to the Oxaya ignimbrites.
222 Intrusion rates greater than about 10 cm/year were required to form a large shallow magma
223 chamber. For a cylindrical magma chamber with radius 20 km this translates into a flux of 0.12
224 km³/year or more. This estimate is comparable to the calculated exchange flow fluxes (Table
225 1) and about two orders of magnitude greater than the 0.001 km³/year needed to generate
226 ~1000 km³ of magma in 1 Myr.

227

228 Finally we discuss incorporation of older crystals into the magmas. Studies of zircon age
229 distributions led to the concept of long periods of cold storage and rapid mobilization of silicic
230 magma into eruptible magma bodies²³. However, preservation of old sanidines rules out cold
231 storage within a non-eruptible mush system at or above the solidus²⁴. Rather the
232 observations indicate catastrophic assimilation and mixing of significant amounts of cold rock.
233 We propose that magma chamber plutonic roof rocks (Figure 4b) disintegrate and are mixed
234 by convection just prior to and during eruption.

235

236 **Data Availability**

237

238 All data are provided as tables ED1 and ED2 in supplementary materials.

239

240 **Code Availability**

241 Code for carrying out the argon diffusion calculations can be found
242 at <https://github.com/Thermochronology-At-Purdue> in the repository named *Oxaya2021*.
243 Code for the Bayesian modelling of the geochronological data is
244 in <https://github.com/brenhinkeller/Chron.jl>. (see reference 65). A file that contains both
245 the script and the data files in the csv format can be downloaded from
246 https://storage.googleapis.com/brenhin/OxayaArArUPb_Chron.tgz
247

248 **References**

- 249 1. Lipman, P.W. Incremental assembly and prolonged consolidation of Cordilleran magma
250 chambers: Evidence from the Southern Rocky Mountain volcanic field. *Geosphere* 3, 42–
251 70, (2007).
- 252 2. Glazner, A. F., Bartley, J. M., Coleman, D. S., Gray, W. & Taylor, R. Z. Are plutons assembled
253 over millions of years by amalgamation from small magma chambers? *Geological Society*
254 *of America Today* 14, 4-12 (2004).
- 255 3. Bachmann, O., Miller, C. & De Silva, S. The volcanic–plutonic connection as a stage for
256 understanding crustal magmatism. *Journal of Volcanology and Geothermal Research* 167,
257 1-23 (2007).
- 258 4. Frazer, R. E., Coleman, D. S. & Mills, R. D. Zircon U-Pb geochronology of the Mount Givens
259 Granodiorite: Implications for the genesis of large volumes of eruptible magma. *Journal*
260 *of Geophysical Research: Solid Earth* 119, 2907-2924 (2014).
- 261 5. Lipman, P. W. & Bachmann, O. Ignimbrites to batholiths: Integrating perspectives from
262 geological, geophysical, and geochronological data. *Geosphere*, GES01091. 01091 (2015).

- 263 6. Charlier, B.L.A., Wilson, C.J.N., Lowenstern, B., Blake, S., van Calsteren P.W. & Davidson,
264 J.P. Magma Generation at a Large, Hyperactive Silicic Volcano (Taupo, New Zealand)
265 Revealed by U–Th and U–Pb Systematics in Zircons. *J Petrology* 46, 3-32 (2005)
- 266 7. de Silva, S.L. & Gosnold, W.D. Episodic construction of batholiths: insights from the
267 spatiotemporal development of an ignimbrite flare-up. *Journal of Volcanology and*
268 *Geothermal Research* 167, 320–335 (2007).
- 269 8. Sparks, R.S.J., Annen, C., Blundy, J.D., Cashman, K.V., Rust, A.C. & Jackson, M.D. Formation
270 and dynamics of magma reservoirs. *Philosophical Transactions of the Royal Society A* 377:
271 20180019 (2019).
- 272 9. Druitt, T.H., Costa, F., Deloule, E., Dungan, M. & Scaillet, B. (2012). Decadal to monthly
273 timescales of magma transfer and reservoir growth at a caldera volcano. *Nature* 482, 77–
274 80 (2012).
- 275 10. Shamloo, H.I. & Till, C.B. Decadal transition from quiescence to supereruption: petrologic
276 investigation of the Lava Creek Tuff, Yellowstone Caldera. *Contributions to Mineralogy*
277 *and Petrology* 174:32 (2019).
- 278 11. Pamukçu, A.S., Wright, K.A., Gualda, G.A.R. & Gravelly, D. Magma residence and eruption
279 at the Taupo Volcanic Center (Taupo Volcanic Zone, New Zealand): insights from
280 rhyolite-MELTS geobarometry, diffusion chronometry, and crystal textures. *Contributions*
281 *to Mineralogy and Petrology* 175:48 (2020).
- 282 12. Rubin, A.E., Kari M. Cooper, K.M., Till, C.B., Kent A.R.J., Costa F., Bose M. Gravelly D.,
283 Deering, C. & Cole J. Rapid cooling and cold storage in a silicic magma reservoir recorded
284 in individual crystals. *Science* 356, 1154–1156 (2017)

- 285 13. Annen, C., Scaillet, B. & Sparks, R.S.J. Thermal constraints on the emplacement rate of a
286 large intrusive complex: the Manaslu Leucogranite, Nepal Himalaya. *Journal of Petrology*
287 47, 71-95 (2006).
- 288 14. Annen, C. From plutons to magma chambers: thermal constraints on the accumulation of
289 eruptible silicic magma in the upper crust. *Earth and Planetary Science Letters* 284, 409-
290 416 (2009).
- 291 15. Annen, C., Blundy, J. D., Leuthold, J. & Sparks, R. S. J. Construction and evolution of igneous
292 bodies: Towards an integrated perspective of crustal magmatism. *Lithos* 230, 206-221
293 (2015).
- 294 16. Gregg, P.M., de Silva, S.L., Grosfils, E.B. & Parmigiani, J.P. Catastrophic caldera-forming
295 eruptions: Thermomechanics and implications for eruption triggering and maximum
296 caldera dimensions on Earth. *Journal of Volcanology and Geothermal Research* 241–242,
297 1–12 (2012).
- 298 17. Paterson, S., Okaya, D., Memeti, V., Economos, R. & Miller R.B. Magma addition and flux
299 calculations of incrementally constructed magma chambers in continental margin arcs:
300 Combined field, geochronologic, and thermal modeling studies. *Geosphere* 7, 1439-1468
301 (2011).
- 302 18. Annen, C., Blundy, J.D. & Sparks, R.S.J. The genesis of intermediate and silicic magmas in
303 deep crustal hot zones. *Journal of Petrology* 47, 505-539 (2006).
- 304 19. Solano, J.M.S., Jackson, M.D., Sparks, R.S.J., Blundy, J.D. & Annen, C. Segregation in Deep
305 Crustal Hot Zones: a Mechanism for Chemical Differentiation, Crustal Assimilation and the
306 Formation of Evolved Magmas. *Journal of Petrology* 53, 1999-2026 (2012).

- 307 20. Cashman K.V., Sparks, R.S.J. & Blundy J. Vertically extensive and unstable crystals mushes:
308 a unifying view of igneous processes associated with volcanoes. *Science* 355, 6331
309 eaag3055 (2017).
- 310 21. Jackson, M. Blundy J. & Sparks R.S.J. Chemical differentiation, cold storage and
311 remobilization of magma in the Earth's crust. *Nature* 564, 405-409 (2018).
- 312 22. Seropian, G., Rust, A. & Sparks, R.S.J. The gravitational stability of lenses in magma
313 mushes: confined Rayleigh-Taylor instabilities. *Journal of Geophysical Research* 123,
314 3593-3607 (2017).
- 315 23. Cashman, K.V. & Giordano, G. Calderas and magma reservoirs. *Journal of Volcanology and*
316 *Geothermal Research* 288, 28-45 (2014).
- 317 24. Cooper, K.M. & Kent, A.J.R. 2014, Rapid remobilization of magmatic crystals kept in cold
318 storage. *Nature* 506, 480-483 (2014).
- 319 25. van Zalinge, M.E., Sparks, R.S.J., Cooper, F.J. & Condon, D. Early Miocene large volume
320 ignimbrites of the Oxaya Formation, Central Andes. *Journal of the Geological Society of*
321 *London* 173, 716-733 (2016).
- 322 26. García, M., Gardeweg, M., Clavero, J. & Hérail, G. 2004. Arica map: Tarapacá Region, scale
323 1:250,000. In: *Carta Geológica de Chile Serie Geología básica*, 84, Servicio Nacional de
324 *Geología y Minería*, Santiago.
- 325 27. van Zalinge, M.E., Sparks, R.S.J. & Blundy, J.D. Petrogenesis of the large-volume Cardones
326 ignimbrite, Chile; development and destabilisation of a complex magma-mush system.
327 *Journal of Petrology* 58, 1975- 2006 (2018).

- 328 28. Freymuth, H., Brandmeier, M. & Wörner, G. The origin and crust/mantle mass balance of
329 Central Andean ignimbrite magmatism constrained by oxygen and strontium isotopes and
330 erupted volumes. *Contributions to Mineralogy and Petrology* 169, 1-24 (2015).
- 331 29. Lissenberg, C. J., Rioux, M., Shimizu, N., Bowring, S. A. & Mével, C. Zircon Dating of Oceanic
332 Crustal Accretion. *Science* 323, 1048–1050 (2009).
- 333 30. Wotzlaw, J.-F. et al. Tracking the evolution of large-volume silicic magma reservoirs from
334 assembly to supereruption. *Geology* 41, 867–870 (2013).
- 335 31. Samperton, K. M., Bell, E. A., Barboni, M., Keller, C. B. & Schoene, B. Zircon age-
336 temperature-compositional spectra in plutonic rocks. *Geology* 45, 983–986 (2017).
- 337 32. Ellis, B. S. et al. Split-grain $^{40}\text{Ar}/^{39}\text{Ar}$ dating: Integrating temporal and geochemical data
338 from crystal cargoes. *Chemical Geology* 457, 15–23 (2017).
- 339 33. Andersen, N.L., Jicha, B.R., Singer, B.S. & Hildreth, W. Incremental heating of Bishop Tuff
340 sanidine reveals pre-eruptive radiogenic Ar and rapid remobilization from cold storage
341 PNAS 114 (47) 12407-12412 (2017).
- 342 34. Pinto, L., Hérail, G., Fontan, F. & Parseval, P. Neogene erosion and uplift of the western
343 edge of the Andean Plateau as determined by detrital heavy mineral analysis.
344 *Sedimentary Geology* 195, 217-237 (2007).
- 345 35. Wotzlaw, J.F., Decou, A., von Eynatten, H., Wörner, G. & Frei, D. Jurassic to Palaeogene
346 tectono-magmatic evolution of northern Chile and adjacent Bolivia from detrital zircon U-
347 Pb geochronology and heavy mineral provenance. *Terra Nova* 23, 399–406 (2011)

- 348 36. Somoza, R. Updated azca (Farallon)—South America relative motions during the last 40
349 My: implications for mountain building in the central Andean region. *Journal of South*
350 *American Earth Sciences* 11, 211-215 (1998).
- 351 37. Isacks, B. L. Uplift of the central Andean plateau and bending of the Bolivian orocline.
352 *Journal of Geophysical Research: Solid Earth* 93, 3211-3231 (1988).
- 353 38. Lamb, S. & Hoke, L. Origin of the high plateau in the Central Andes, Bolivia, South America.
354 *Tectonics* 16, 623-649 (1997).
- 355 39. Kay, S. M. & Coira, B. L. Shallowing and steepening subduction zones, continental
356 lithospheric loss, magmatism, and crustal flow under the Central Andean Altiplano-Puna
357 Plateau. *Geological Society of America Memoirs* 204, 229-259 (2009).
- 358 40. Hora, J. M., Singer, B. S., Jicha, B. R., Beard, B. L., Johnson, C. M., de Silva, S. & Salisbury,
359 M. Volcanic biotite-sanidine $^{40}\text{Ar}/^{39}\text{Ar}$ age discordances reflect Ar partitioning and pre-
360 eruption closure in biotite. *Geology* 38, 923-926 (2010).
- 361 41. Platzman, E.S., Sparks, R.S.J. & Cooper, F.J. Fabrics, facies and flow through a large-volume
362 ignimbrite: Pampa De Oxaya, Chile. *Bulletin of Volcanology* 82:8 (2020).
- 363 42. Schöpa, A. & Annen, C. The effects of magma flux variations on the formation and lifetime
364 of large silicic magma chambers. *Journal of Geophysical Research: Solid Earth* 118, 926-
365 942 (2013).
- 366 43. Schöpa A., Annen, C., Dilles, J.H., Sparks R.S.J. & Blundy, J.D. Magma Emplacement Rates
367 and Porphyry Copper Deposits: Thermal Modeling of the Yerington Batholith. *Economic*
368 *Geology* 112, 1653-1672 (2018).

369 44. Burgmann, R. & Dresen, G. Rheology of the Lower Crust and Upper Mantle: Evidence from
370 Rock Mechanics, Geodesy, and Field Observations. *Annual Reviews of Earth & Planetary*
371 *Sciences* 36, 531-567 (2008).

372 45. Burov, E., Jaupart, C. & Guillou-Frottier, L. Ascent and emplacement of buoyant magma
373 bodies in brittle-ductile upper crust. *Journal of Geophysical Research: Solid Earth*, 108(B4)
374 (2003).

375 46. Petford, N., Cruden, A.R., McCaffrey, K.J.W. & Vigneresse, J.L. Granite magma formation,
376 transport and emplacement in the Earth's crust. *Nature* 408, 669–673 (2000).

377 47. Suckale, J., Qin, Z., Picchi, D., Keller, T., & Battiato, I. (2018). Bistability of buoyancy-driven
378 exchange flows in vertical tubes. *Journal of Fluid Mechanics*, 850, 525-550.

379
380
381

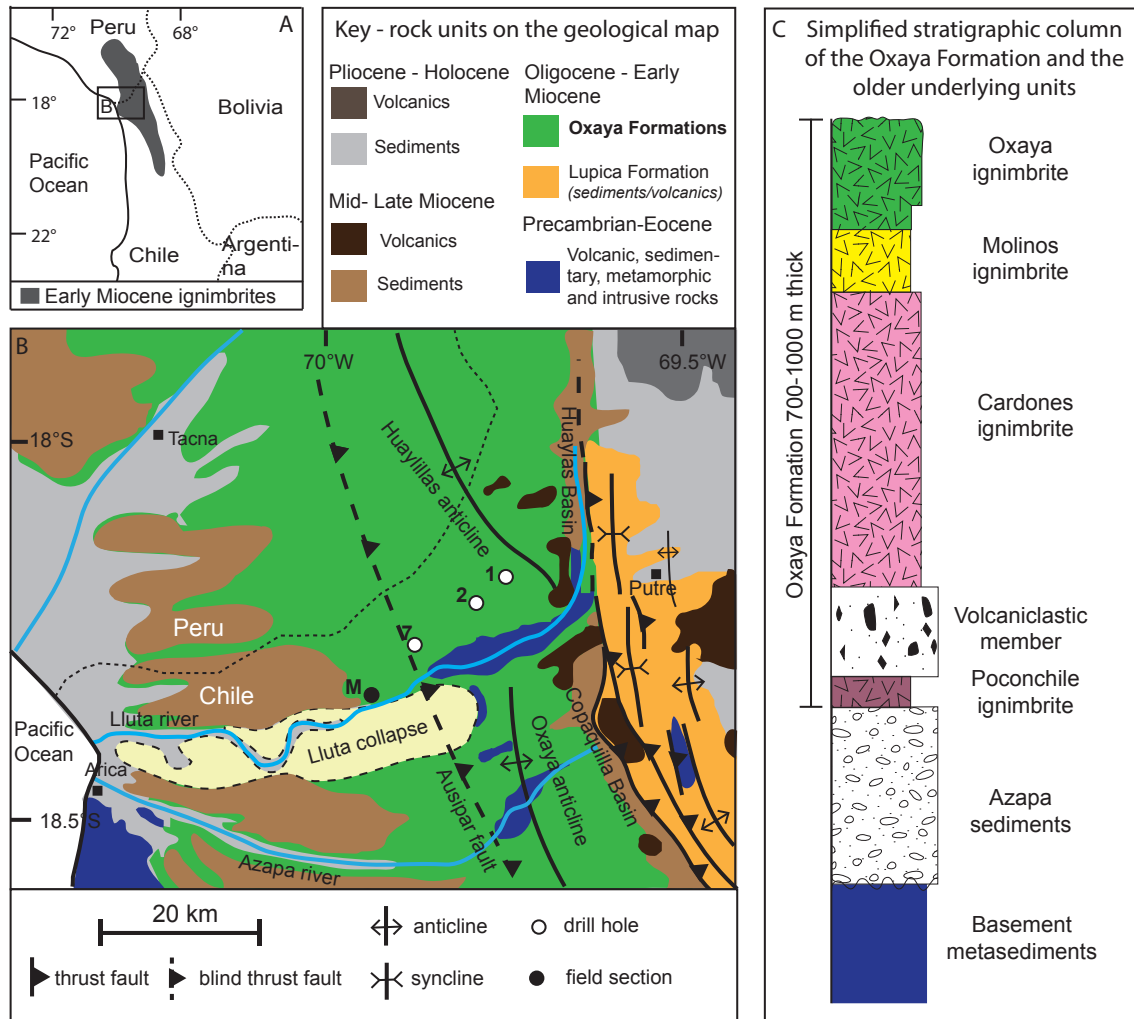
Crustal radius (km)	Conduit radius (m)	Magma flux (km ³ /yr)	Magma volume (km ³)	Assembly time (years)
15	4.7	0.18	710	3800
20	6.3	0.58	1300	2200
25	7.9	1.40	2000	1400

382
383 Table 1. Results of calculations for exchange flow. Calculations are shown for the flow up a
384 cylindrical conduit and are rounded to 2 significant figures. Results are shown for conduit
385 radius, magma flux, magma chamber volume and magma chamber assembly times for a melt

386 layer 1 km thick with crustal viscosity $\mu_c = 10^{19}$ Pa s. Calculations for three different radius
387 values of the magma system (See Figure 4) are presented.
388

389 Figures

390



391

392 Figure 1. (A) Location of study area in Central Andes with distribution of early Miocene

393 ignimbrites. (B) Simplified geological map of study area showing distribution of the Oxaya

394 Formation and major structural features in the area modified by van Zalinge et al.²⁵ after

395 Garcia et al.²⁶ (C) Simplified stratigraphy²⁴ of the Oxaya Formation and underlying

396 stratigraphic units based on locality M and drill hole data (B).

397

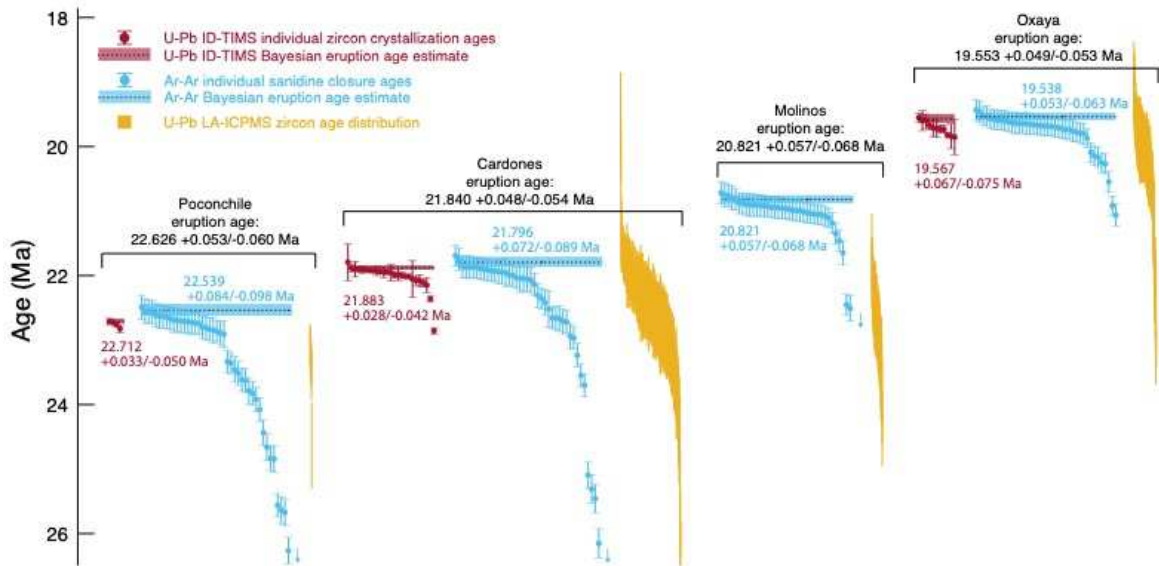
398

399

400

401

402



403

404 Figure 2. Geochronological data for the four ignimbrites of the Oxaya Formation. Four kinds

405 of data are shown: U-Pb ages (ID-TIMS) of individual euhedral zircons; Ar-Ar ages of individual

406 sanidine fragments; and U-Pb ages (LA-ICPMS) of individual inherited zircons. The fourth

407 preferred age comes about from integration of the U-Pb ages of zircons and Ar/Ar ages of

408 sanidines. The data are ordered by age from left (youngest) to right (oldest). The error bars

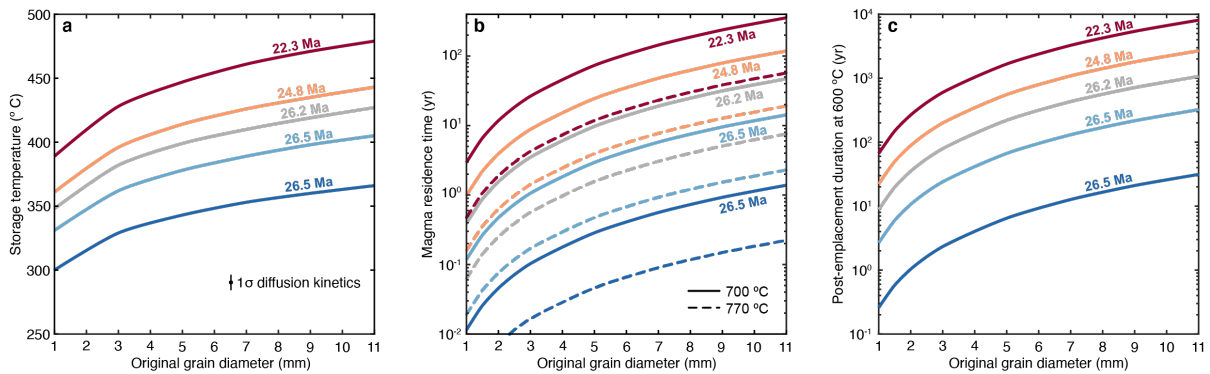
409 on data points are 2 standard deviation values.

410

411

412

413



414

415 Figure 3. Models of the effects of (A) storage temperatures, (B) magma residence times, and

416 (C) post-emplacment welding and cooling of the ignimbrites on sanidine $^{40}\text{Ar}/^{39}\text{Ar}$ ages in

417 the cores of sanidine crystals. We show model ages for the cores of crystals, where the core

418 is defined as a the volume at the center of the original crystal that has a diameter that is 50%

419 that of the original crystal. We show $^{40}\text{Ar}/^{39}\text{Ar}$ ages of crystal cores for two reasons. First, we

420 know that the $^{40}\text{Ar}/^{39}\text{Ar}$ measurements were made on sanidine crystal fragments, and that

421 the grains were fragmented during the mineral separation process. Second, diffusive loss of

422 ^{40}Ar will cause rim-to-core age gradients; therefore it is the crystal cores that will provide the

423 oldest ages in our observed $^{40}\text{Ar}/^{39}\text{Ar}$ age distributions. For each set of models, we assume

424 that all sanidines crystallized at 26.5 Ma and that eruption occurred at 21.8 Ma. (A) Modeled

425 sanidine crystal core $^{40}\text{Ar}/^{39}\text{Ar}$ age as a function of original grain size and storage temperature.

426 (B) Modeled sanidine crystal core $^{40}\text{Ar}/^{39}\text{Ar}$ age as a function of original grain size and magma

427 residence time, assuming that no diffusive ^{40}Ar loss occurred prior to magma entrapment.

428 Models are shown for two magma temperatures – 700 and 770°C, based on

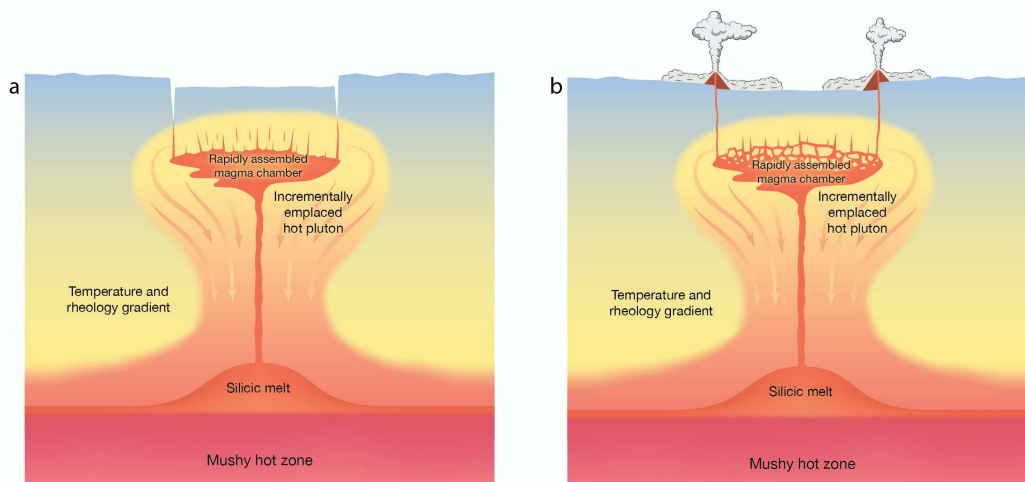
429 geothermometry²⁶. (C) Modelled sanidine crystal core $^{40}\text{Ar}/^{39}\text{Ar}$ age at 600°C, the maximum

430 temperature during post-emplacment welding and cooling of the ignimbrites, assuming no

431 prior diffusive ^{40}Ar loss during pre-eruption storage or magma residence.

432

433



434

435 Figure 4. Simplified conceptual model of a transcrustal magmatic system involving
436 segregation of silicic melt from a middle to lower crustal hot zone, incipient Rayleigh Taylor
437 instability and transfer to an upper crustal magma chamber by a dyke. depiction is after the
438 incubation period in which a large batholith system has been emplaced in the upper crust and
439 hosts the development of the large magma chamber. In (a) the shallow magma chamber is
440 being emplaced prior to eruption and in (b) the surrounding co-genetic earlier plutonic rocks
441 are disrupted and incorporated into the erupting magma chamber.

442

443

444

445

Methods (words 2882)

446 *Magma system Terminology*

447 A transcrustal igneous system spans the mantle to the surface and includes magma chambers,
448 igneous mush at or above the solidus and fully solidified cognate igneous rocks below the
449 solidus, as well as host rocks consumed or intimately incorporated into the system by
450 intrusive mechanisms. Mush is defined as a mixture of melt and crystals forming an
451 interconnected framework in any proportions⁸, while magma is defined as melt regions
452 containing suspended crystals. The transition between mush and magma occurs over crystal
453 contents of typically 50-60%. A magma reservoir is that part of the system containing melt.
454 Mechanisms of forming large bodies of magma (chambers)⁸ include: incremental intrusion at
455 flux rates sufficient to sustain high enough temperatures for magma formation¹⁴; segregation
456 of evolved melts at the top of or within mushes^{19,21,48}; amalgamation of smaller-scale melt-
457 rich layers within mushes to form larger-volume magma bodies²³; reheating of mush or fully
458 solidified igneous rocks⁴⁹; and fluxing of higher-temperature fluids transferred from hotter
459 mafic magmas^{50,51}. Finally, super-eruptions are defined as eruptions of magnitude 8 or
460 greater involving at least 10^{15} kg of magma⁵².

461

462 *Geochronology*

463 ⁴⁰Ar/³⁹Ar ages were obtained from feldspar phenocrysts. Briefly, pyroclasts were crushed in a
464 jaw crusher, sieved, washed repeatedly in de-ionized water, before magnetically separated
465 to isolate feldspar phenocrysts. The feldspar phenocrysts were leached in an ultrasonic bath
466 in 5% HF for 5 minutes to remove adhering groundmass glass, before being rinsed three times

467 in de-ionized water in an ultrasonic bath. Once dried, the feldspars were passed through a
468 magnetic separator at low speed and low angle of tilt, to remove feldspar phenocrysts with
469 mineral or melt inclusions. Samples were then hand-picked under a binocular microscope to
470 eliminate any remaining crystals containing inclusions and any visibly altered crystals.
471 Sanidine crystals were harvested from individual pumice clasts and pumice fiamme from the
472 Cardones and Molinos ignimbrites to avoid contamination with accidental crystals picked up
473 from the conduit and surface during the eruption. This, however, was not possible for the
474 fine-grained Poconchile and Oxaya ignimbrites; we isolated sanidines from the bulk rock from
475 ignimbrites samples with very low lithic contents to minimize contamination. Many of the
476 sanidines from the Oxaya Formation are distinctively rich in Ba or have Ba-rich growth zones,
477 so we are confident that almost all the sanidines are cognate with the magmatic system, an
478 interpretation which was confirmed *a posteriori*. Our samples are typically ~2 mm in
479 dimension but may be fragments of larger crystals as petrography indicated that sanidine
480 crystals up to 12 mm are common²⁶. 50 individual sanidine crystals from each ignimbrite for
481 laser fusion ⁴⁰Ar-³⁹Ar geochronology. Details of the samples and results are given in Table M1.
482 The data table for ⁴⁰Ar-³⁹Ar geochronology results (Table ED1) is in supplementary materials.
483

484 Pristine crystals were parcelled into Cu packets, or Al discs, stacked in glass vials and sealed
485 in a large glass vial for irradiation. International standard Fish Canyon sanidine (FCs; with an
486 age of 28.294 ± 0.0036 Ma) were used as fluence monitors for J-determination and packaged
487 throughout the stack at known spacing (geometry) in between samples. Samples and
488 standards were irradiated at the Cd-lined (CLICIT) facility of the Oregon State University (USA)
489 TRIGA reactor for 15.02 hours. Single irradiated crystals ($n= 30$ per sample) were fused with

490 a CO₂ laser and isotope data were collected using a MAP 215-50 noble gas mass
491 spectrometer⁵².

492

493 Samples were analyzed in a single batch; backgrounds and mass discrimination
494 measurements (via automated analysis of multiple air pipettes) specific to each batch were
495 used to correct the data. Air pipettes were run (on average) after every 4 analyses.
496 Backgrounds subtracted from ion beam measurements were arithmetic averages and
497 standard deviations. These were measured after every analysis. Mass discrimination was
498 computed based on a power law relationship⁵³ using the isotopic composition of atmospheric
499 Ar reported by Lee et al.⁵⁵ that has been independently confirmed⁵⁶. Corrections
500 for radioactive decay of ³⁹Ar and ³⁷Ar were made using published decay constants^{57,58}.
501 Ingrowth of ³⁶Ar from decay of ³⁶Cl was corrected using the ³⁶Cl/³⁸Cl production ratio and
502 methods of Renne et al.⁵⁹ and was determined to be negligible.

503

504 The samples were analyzed by total fusion and step-heating with a CO₂ laser. The mass
505 spectrometer is equipped with a Nier-type ion source. The MAP 215-50 data were collected
506 using an analogue electron multiplier detector. Mass spectrometry utilized peak-hopping by
507 magnetic field switching for 10 cycles.

508

509 Ages were computed from the blank-, discrimination- and decay-corrected Ar isotope data
510 after correction for interfering isotopes based on the following production ratios, determined
511 from fluorite and Fe-doped KAlSiO₄ glass: (³⁶Ar/³⁷Ar)_{Ca} = (2.650 ± 0.022) × 10⁻⁴; (³⁸Ar/³⁷Ar)_{Ca} =
512 (1.96 ± 0.08) × 10⁻⁵; (³⁹Ar/³⁷Ar)_{Ca} = (6.95 ± 0.09) × 10⁻⁴; (⁴⁰Ar/³⁹Ar)_K = (7.3 ± 0.9) × 10⁻⁴;

513 $(^{38}\text{Ar}/^{39}\text{Ar})_{\text{K}} = (1.215 \pm 0.003) \times 10^{-2}$; $(^{37}\text{Ar}/^{39}\text{Ar})_{\text{K}} = (2.24 \pm 0.16) \times 10^{-4}$, as determined
514 previously for this reactor in the same irradiation conditions⁶⁰. Ages and their uncertainties
515 are based on the methods of Renne et al.⁶¹, the calibration of the decay constant⁶² and the
516 FCs optimization age. The optimization-modeled age has accurate quantifiable uncertainties
517 and hence is favored here over the astronomically tuned FCs ages⁶³. The reason for this
518 preference is that the astronomical calibration has unknown uncertainty and confidence
519 intervals and uses best guess ‘assumptions’ to constrain, for example, phase relationships
520 between insolation and climate.

521

522 For the age comparisons made herein, contributions from sources of systematic uncertainty
523 (i.e., uncertainties in $^{40}\text{Ar}/^{40}\text{K}$ of the standard and ^{40}K decay constants) are neglected and only
524 analytical uncertainties in isotope measurements of samples and standards are included⁶⁴.
525 These uncertainties are referred to herein as “analytical precision”. For the purposes of this
526 study analytical uncertainties include contributions from uncertainties in the interference
527 corrections because these interference corrections have variable effects due to the slight
528 variable chemistry of the samples considered.

529

530 Zircon ages of three of the Oxaya ignimbrites have been previously presented²⁵. These ages
531 were determined by single-crystal zircon U-Pb CA-ID-TIMS $^{206}\text{Pb}/^{238}\text{U}$ analyses of high aspect
532 ratio zircons lacking any complex crystal shapes and evidence of older cores. Zircons with
533 inherited cores were excluded from the U–Pb ID-TIMS $^{206}\text{Pb}/^{238}\text{U}$ analyses that contributed to
534 the estimates of eruption age. They were instead analysed by LA-ICPMS. These zircon crystals
535 are complex with resorbed cores. Ages determined by LA-ICPMS from inherited zircons

536 (Figure 2) reveal highly dispersed age spectra (MSWD >7 for samples with >50 analyses, even
 537 excluding antecrysts).

538

539 We investigated zircons from each unit that had been screened out from the single crystals
 540 study eruptions age study. These excluded zircons included anhedral crystals with complex
 541 shapes and zircons with cores. This population subset was analysed by LA-ICPMS U-Pb.
 542 Zircons were analysed at the Geochronology & Tracers Facility, British Geological Survey (GTF-
 543 BGS) using a Nu Instruments, Nu Plasma HR, multi-collector inductively coupled plasma mass
 544 spectrometer (MC-ICP-MS). The Nu Plasma HR was operated in static mode, with
 545 simultaneous measurement of the isotopes of interest on either a Faraday detector or an ETP
 546 secondary electron multiplier (see Table M2 below).

547

ExH	H6	H4	H3	H2	H1	Ax	L1	L2	IC0	IC1	L3	IC2	L4	L5 ^{*1}
²³⁸ U	²³⁵ U	-	-	-	-	-	-	-	²⁰⁷ Pb	²⁰⁶ Pb	-	²⁰⁴ Pb ²⁰⁴ Hg	-	²⁰² Hg
Detectors not in use														

548

549

550 **Table M2:** Configuration of the Nu Plasma HR ‘Zircon’ block used for U-Pb geochronology at
 551 GTF-BGS. ^{*1} measured to allow for the correction of ²⁰⁴Hg on ²⁰⁴Pb. H denotes high mass
 552 Faraday collectors, L denotes low mass Faraday collectors and IC denotes ion counter
 553 detectors.

554

555 Laser sampling was performed using a New Wave Research 193nm laser ablation system,
 556 incorporating an in-house designed, low-volume sample cell with an ablation volume of ca.
 557 3-4 cm³, which, when combined with ~1m tubing to the plasma torch, leads to a signal
 558 washout time of ~ 1 second. The ablation parameters were as follows: 35µm static spot, run

559 at a repetition rate of 10Hz, with a fluence of $\sim 2.2\text{J}/\text{cm}^2$. Samples were ablated for 30 seconds
560 with a 15 second washout/laser warm-up period between each analyses.

561

562 Data were acquired using the time-resolved analysis function of the Nu HR's software, and
563 processed using Lolite; a software package specifically designed to handle the large volumes
564 of data produced by LA-ICP-MS. Lolite employs the 'standard-sample-bracketing' technique
565 to correct the data. This involves the calculation of a normalisation factor (measured/known)
566 for both the $^{207}\text{Pb}/^{206}\text{Pb}$ and $^{206}\text{Pb}/^{238}\text{U}$ of a primary zircon reference material (91500; $1062 \pm$
567 0.4 Ma), which is analysed at regular intervals during each session. These normalization
568 factors were then applied to the sample data. Two other zircon reference materials (GJ1 and
569 Mud Tank, $602 \pm 1\text{Ma}$ and 732 ± 5 Ma, respectively) were also analysed during each session,
570 to check the accuracy and precision of this method.

571

572 Table ED2 in supplementary materials provides information on the individual ICP-MS zircon
573 analyses.

574

575 The propagated uncertainties were produced by Lolite and reflect the quadratic combination
576 of the internal uncertainty, (i.e. the reproducibility of the measured ratios) with the external
577 uncertainty (i.e. the reproducibility of the bracketing reference material). Components
578 relating to the systematic uncertainty of the method (i.e. age uncertainty of the primary
579 reference material, decay constant uncertainties and the long-term variance of the secondary
580 reference material) are quadratically added, post Lolite, using an in-house Excel spreadsheet.

581

582 Dispersed $^{40}\text{Ar}/^{39}\text{Ar}$ and U-Pb age distributions (Figure 2) preclude the calculation of a
583 traditional weighted mean, leading us to adopt a Bayesian approach to eruption age
584 estimation based on the algorithm of Keller et al.⁶⁵. For either mineral, Bayesian eruption age
585 estimation requires a prior estimate of the *relative age distribution* of crystallization (zircon)
586 or apparent closure (sanidine) ages prior to eruption, which may be estimated either
587 petrologically (e.g. zircon saturation modelling) or by bootstrapping⁶⁶. Since the geological
588 process driving pre-eruptive age heterogeneity in sanidine is not yet well understood, we
589 must begin with a bootstrapping approach.

590

591 Incorporating all available $^{40}\text{Ar}/^{39}\text{Ar}$ age distributions that feature well-resolved pre-eruptive
592 heterogeneity, bootstrapping by kernel density estimation reveals (Figure S1) a consistent,
593 exponential form of the relative closure age distribution. This exponential form suggests an
594 underlying survivorship process (e.g. potentially consistent with geologic processes ranging
595 from partial degassing of xenocrystic sanidine entrained during eruption to pre-eruptive Ar
596 accumulated in a cold-storage regime. We note that for excess Ar a continuum of ages as
597 observed would not be expected. When cast on an isotope correlation plot, the Ar/Ar data
598 define isochrons with atmospheric $^{40}\text{Ar}/^{36}\text{Ar}$, albeit at relatively low precision owing to the
599 high radiogenic Ar content. Using this bootstrapped relative closure age distribution, the
600 resulting eruption age estimates based on $^{40}\text{Ar}/^{39}\text{Ar}$ sanidine ages for the Cardones are
601 indistinguishable within uncertainty from those based on U-Pb CA-ID-TIMS zircon
602 crystallization ages (Table MD1), whereas the $^{40}\text{Ar}/^{39}\text{Ar}$ sanidine ages for Poconchile and
603 Oxaya ignimbrites are just beyond uncertainty of each other. To account for this we calculate
604 an integrated $^{40}\text{Ar}/^{39}\text{Ar}$ and U-Pb age.

605

606 We re-calculated the previous zircon ages²⁵ using the Bayesian method. Incorporating
607 constraints from both sanidine and zircon eruption age estimates, we also estimate the
608 repose intervals between eruptions as illustrated in Figure S2, using the superposition
609 algorithm of Keller⁵⁴.

610

611 We first estimated empirically the form of the *relative closure distribution*, analagous to
612 the *relative crystallization distribution* of Keller et al.⁶⁶ using a method equivalent to the
613 "bootstrapping" approach⁶⁷. The results (Figure S1) revealed a characteristic form of the
614 closure distribution featuring a nearly exponential decrease in probability density with
615 increasing time prior to eruption. The consistency and reproducibility of this form, to first
616 order, between all available well-resolved single-crystal volcanic sanidine Ar-Ar age
617 distributions (both from the Andean ignimbrites of this study, and the Mesa Falls Tuff⁶⁷)
618 suggests that this exponential form may be underlain by a consistent physical process. A
619 survivorship process wherein, for example, each sanidine has some finite probability of being
620 reset by reheating in any given pre-eruptive time interval — would provide one simple
621 mechanism for producing such an exponential trend.

622

623 We then applied the Markov chain Monte Carlo eruption age estimation algorithm in the
624 Chron.jl software package⁶⁵ to each ignimbrite, using a half-Normal relative crystallization
625 distribution for all ID-TIMS zircon ages, and our previously determined exponential relative
626 closure distribution for all sanidine Ar-Ar ages, as illustrated in Figure S2. Systematic
627 uncertainties were propagated using the "optimization intercalibration" the constants of
628 Renne et al.⁶² for Ar-Ar ages, and the decay constants of Jaffey et al.⁶⁸ along with the effective
629 systematic uncertainty of the EarthTime tracer^{69,70} for U-Pb TIMS ages. Finally, to estimate

630 the durations of the repose intervals between each ignimbrite (Figure S2), we used Chron.jl
631 to run a second “stratigraphic” MCMC model, combining both the new eruption age estimates
632 and the relative age constraints provided by the stratigraphic superposition of the
633 ignimbrites. Table M1 shows all model outputs.

634

635

636 *Diffusion modeling*

637 Argon diffusion calculations were carried out using analytical solutions for simultaneous
638 production and diffusion^{71,72}. These solutions, which involve two infinite series, typically
639 converge with less than 20 partial sums. We use measured argon diffusion kinetics for Fish
640 Canyon sanidine⁷³. We assume that all sanidine crystals form at 26.5 Ma, reside at a constant
641 temperature until 21.8 Ma (the approximate eruption age of Cardones) and experience no
642 ⁴⁰Ar diffusive loss after eruption. In the case of magma residence times, we also assume that
643 no argon diffusion occurs during cold storage (i.e., that ⁴⁰Ar concentration profiles in sanidine
644 crystals were uniform at the beginning of magma residence). Because some prior diffusive
645 rounding of the ⁴⁰Ar concentration profiles likely occurred during cold storage, our estimates
646 of magma residence times should be considered minima.

647

648 Uncertainties in cold storage temperatures due to uncertainties in argon diffusion kinetics are
649 fairly invariant and range from ± 5 to ± 6 °C (1σ), with the largest uncertainties corresponding
650 to small grain sizes and low degrees of fractional argon loss (i.e., older ⁴⁰Ar/³⁹Ar ages). Because
651 magma residence times range over a few orders of magnitude, absolute uncertainties in
652 magma residence times due to uncertainties in argon diffusion kinetics also range over a few

653 orders of magnitude. Generally, magma residence time uncertainty increase with increasing
654 and degree of fractional argon loss (i.e., younger $^{40}\text{Ar}/^{39}\text{Ar}$ ages), increasing grain size, and
655 decreasing magma residence temperature. Relative uncertainties in magma residence times,
656 on the other hand, are essentially invariant with grain size or degree of fractional loss, and
657 are $\sim 7\%$ for residence temperatures of $700\text{ }^\circ\text{C}$ and $\sim 3\%$ for residence temperatures of $770\text{ }^\circ\text{C}$.
658 For example, for an 11 mm-diameter sanidine grain that experienced 96% fractional loss (i.e.,
659 has an $^{40}\text{Ar}/^{39}\text{Ar}$ age of 22 Ma), the residence time at $700\text{ }^\circ\text{C}$ is 356 ± 25 years, while the
660 residence time at $770\text{ }^\circ\text{C}$ is 57 ± 2 years.

661

662 *Magma transport modelling*

663 We apply here an experimentally verified model for the development of buoyancy induced
664 instability for a growing melt layer beneath a layer of much greater viscosity²². Here a silicic
665 melt layer extracted from an underlying mush accumulates beneath hot upper crust (Figure
666 4). The wavelength of the fastest growing RT instability in the case of an unconfined layer is
667 given by;

668

$$669 \quad \lambda = 9.058 \left(\dot{h} / \Delta\rho g \right)^{1/2} \mu_m^{1/6} \mu_c^{2/3} \quad (\text{M1})$$

670

671 where \dot{h} is the growth rate of the unstable layer, g is gravity, $\Delta\rho$ is the density difference
672 between melt and overlying crust, μ_m is the viscosity of the silicic melt layer, and μ_c is the
673 viscosity of overlying hot just sub-solidus crust. Representative values are $\Delta\rho = 300\text{ kg/m}^3$, μ_m
674 $= 10^5\text{ Pa s}$, and $\mu_c = 10^{19}\text{ Pa s}$ ⁴². We take \dot{h} values of 1 mm and 5 mm/year based on models
675 of reactive flow related to basalt underplating²⁰ resulting in λ values of 600 and 1400 km.

676 Although approximate these calculations show that the fastest growing wavelength is much
677 larger than the width of zones of magma generation beneath batholiths, taken here to be
678 typically in the range 30 to 50 km. Thus we have applied the theory for confined instability
679 growth²¹ for $\mu_m \ll \mu_c$ to calculate a characteristic time scales for instability:

680

$$681 \quad \tau = (6\pi\mu_c)/(\Delta\rho g D) \quad (M2)$$

682

683 During experiments described in Seropian et al.²² we observed from 16 experiments covering
684 a wide range of material properties (analogue melt layer thicknesses, μ_c and $\Delta\rho$) that the time
685 it takes an instability to transform into a detached diapir was about 4 greater than τ , leading
686 to equation (1) in the main text.

687

688 One possibility is that the RT instability grows to form a diapir which traverses the intervening
689 plutonic crust. However, magma transport by diapirism is too slow to explain the rapid
690 assembly of magma chambers prior to ignimbrite eruptions: we estimate using equation 8 in
691 Burov et al.⁴⁵ that a 1000 km³ diapir with $\Delta\rho = 300 \text{ kg/m}^3$ takes $\sim 10^5$ years to rise 10 km in a
692 crust with an effective viscosity of 10^{19} Pa s . This simplified calculation does not consider heat
693 loss from the diapir, which locally reduces the viscosity of the surroundings⁴⁴, which in turn
694 enables somewhat faster ascent and could help assimilate older plutonic material into the
695 diapir as it ascends. Although this mechanism could explain the spectrum of zircon ages it is
696 not consistent with the abundant old sanidines. Thus dyke transport⁴⁶ provides an attractive
697 mechanism to enable fast magma chamber assembly.

698

699 In our conceptual model (Figure 4) a conduit (dyke or cylinder) is formed that allows an
700 exchange flow⁴⁷ between the middle crustal melt layer and an upper crustal region in which
701 a magma chamber forms. Here we envisage that upward flow of magma along the conduit is
702 balanced by the downward subsidence of the crust. We are interested in the case where the
703 cross-sectional area of the magma conduit is much less than the area of crust flowing
704 downwards ($A_m \ll A_c$) and the magma is much less viscous than the crust ($\mu_m \ll \mu_c$). In this
705 scenario the average speed of the crust downward (U_c) is less than the average magma flow
706 speed up the conduit: $U_c \approx (A_m / A_c) U_m$ by many orders of magnitude. To develop a very
707 simple model we represent the subsiding crust as a large cylinder of radius R and the conduit
708 as a small cylinder of radius r ; note that for a dyke with a length 1000 times its width, its width
709 is approximately a quarter of the radius r of a cylindrical conduit that would accommodate
710 the same flux. Due to the low crust velocity and the large viscosity contrast, the upward flow
711 of magma is well approximated by flow through a cylinder with solid walls (Poiseuille flow):

712

$$713 \quad Q = [\pi r^4 \Delta \rho g] / 8 \mu_m \quad (M3)$$

714

715 where Q is the magma flux (volume/time) through the conduit. Approximating the downward
716 flow as Poiseuille flow with radius R also with flux Q , results in the following relationship:

717

$$718 \quad r = (\mu_m / \mu_c)^{1/4} R \quad (M4)$$

719

720 We have applied equations to make the calculations presented in Table 1. We note that the
721 difference between an exchange flow along a cylinder and a dyke is a matter of geometry
722 with viscous friction being a factor of a few greater in a dyke with the same cross-sectional

723 area as a cylinder. The length of the dyke is an additional factor in governing friction and
724 different choices could be made, but would have a minor effect on calculated magma fluxes.
725 Thus the essential elements of exchange flow are captured by a cylindrical conduit. Even for
726 a cylindrical geometry the calculations presented are approximate and intended only to
727 illustrate the feasibility of the crust subsiding slowly over a large area allowing an exchange
728 flow with relatively fast ascent of magma from the mid- to the upper crust.

729

730 *Methods References*

731

732 48. Jackson, M. D., Cheadle, M. J. & Atherton, M. P. Quantitative modeling of granitic melt
733 generation and segregation in the continental crust. *Journal of Geophysical Research* 108,
734 2332-2353(2003).

735 49. Huppert, H.E. & Sparks, R.S.J. The generation of granite by intrusion of basalt into the
736 continental crust. *Journal of Petrology* 29, 599-624 (1988).

737 50. Bachmann, O. & Bergantz, G. W. Gas percolation in upper crustal silicic crystal mushes
738 as a mechanism for upward heat advection and rejuvenation of near-solidus magma bodies.
739 *Journal of Volcanology and Geothermal Research* 149, 85-102 (2006).

740 51. Huber, C., Bachmann, O. & Manga, M. Two Competing Effects of Volatiles on Heat
741 Transfer in Crystal-rich Magmas: Thermal Insulation vs Defrosting. *Journal of Petrology* 51,
742 847-867 (2010).

743 52. Mason, B., Pyle, D. & Oppenheimer, C. The size and frequency of the largest explosive
744 eruptions on earth. *Bulletin of Volcanology* 66, 735-748 (2004).

745 53. Mark, D.F., Petraglia, M., V.C. Smith, Morgan, L.E., Barfod, D.N., Ellis, B.S. N.J.Pearce,
746 Pal, J.N. & Korissetar, R. A high-precision $^{40}\text{Ar}/^{39}\text{Ar}$ age for the Young Toba Tuff and dating

747 of ultra-distal tephra: forcing of Quaternary climate and implications for hominin occupation
748 of India. *Quaternary Geochronology* 21, 90-103 (2014).

749 54. Renne, P.R. Cassata, W.S. & Morgan, L.E. The isotopic composition of atmospheric
750 argon and $^{40}\text{Ar}/^{39}\text{Ar}$ geochronology: time for a change? *Quaternary Geochronology* 4, 288-
751 298 (2009).

752 55. Lee, J.Y. Marti, K., J.P. Severinghaus, J.P., Kawamura, K., Yoo, H.S., Lee, J.B. & Kim, J.S.
753 A redetermination of the isotopic abundances of atmospheric Ar
754 *Geochimica et Cosmochimica Acta* 70, 4507-4512 (2006)

755 56. D.F. Mark, D.F., Stuart, F.M., & de Podesta, M. New high-precision measurements of
756 the isotopic composition of atmospheric argon. *Geochimica et Cosmochimica Acta* 75, 7494-
757 7501 (2011).

758 57. Stoenner, R.W., Schaeffer, O.A. & Katcoff, S. Half-lives of argon-37, argon-39, and
759 argon-42. *Science* 148, 1325- 132 (1965).

760 58. Renne, P.R. & Norman, E.B. Determination of the half-life of ^{37}Ar by mass
761 spectrometry. *Physics Reviews C* 63, 047302 (2001).

762 59. Renne, P.R., Sharp, Z.D. & Heizler, M.T. Cl-derived argon isotope production in the
763 CLICIT facility of OSTR reactor and the effects of the Cl-correction in $^{40}\text{Ar}/^{39}\text{Ar}$
764 geochronology. *Chemical Geology* 255. 463-466 (2008).

765 60. Renne P.R. Some footnotes to the optimization-based calibration of the $^{40}\text{Ar}/^{39}\text{Ar}$
766 system. *Geological Society London Special Publication* 378, 21-31 (2014).

767 61. Renne, P.R., Mundil, R., Balco, G., Min, K. & Ludwig, K.R. Joint determination of ^{40}K
768 decay constants and $^{40}\text{Ar}^*/^{40}\text{K}$ for the Fish Canyon sanidine standard, and improved
769 accuracy for $^{40}\text{Ar}/^{39}\text{Ar}$ geochronology. *Geochimica et Cosmochimica. Acta* 74, 5349-5367
770 (2010).

- 771 62. Renne, P.R., Mundil, R., Balco, G., Min, K., Ludwig K.R. Response to the comment by
772 W. H. Schwarz et al. on “Joint determination of 40K decay constants and $40\text{Ar}^*/40\text{K}$ for the
773 Fish Canyon sanidine standard, and improved accuracy for $40\text{Ar}/39\text{Ar}$ geochronology.
774 *Geochimica et Cosmochimica Acta* 75, 5097-5100 (2011).
- 775 63. Kuiper, K.F., Deino, A., F.J. Hilgen, F.J., Krijgsman, Renne, P.R. & Wijbrans, J.R.
776 Synchronizing rock clocks of Earth history. *Science* 320, 500-504 (2008).
- 777 64. Mark, D.F., Renne, P.R. Dymock, R.C., Smith, V.C., Simon, J.I., Morgan, L.E. Saff, R.A.,
778 Ellis, B.S. & Pearce, N.J.G. High precision $40\text{Ar}/39\text{Ar}$ dating of Pleistocene tuffs and temporal
779 anchoring of the Matuyama-Brunhes Boundary. *Quaternary Geochronology* 39, 1-23 (2017).
- 780 65. Keller, C.B. Chron.jl: A Bayesian framework for integrated eruption age and age-depth
781 modelling. <https://doi.org/10.17605/osf.io/TQX3F> (2018).
- 782 66. Keller, C. B., Schoene, B. & Samperton, K. M. A stochastic sampling approach to zircon
783 eruption age interpretation. *Geochemical Perspectives Letters* 8, 31–35 (2018).
- 784 67. Ellis, B.S., Mark, D.F., Troch J., Bachmann, O., Guillong, M, Kent, A.J.R. & von Quadt, A.
785 Split-grain $40\text{Ar}/39\text{Ar}$ dating: Integrating temporal and geochemical data from crystal
786 cargoes. *Chemical Geology* 457, 15-23 (2017).
- 787 68. Jaffey, A.H., Flynn, K.F., Glendenin, L.E., Bentley, W.C. & Essling, A.M. Precision
788 Measurement of Half-Lives and Specific Activities of ^{235}U and ^{238}U . *Physics Reviews C* 4,
789 1889 (1971).
- 790 69. Condon, D.J., Schoene, B., McLean, N.M., Bowring, S.A. & Parrish, R.R. Metrology and
791 traceability of U–Pb isotope dilution geochronology (EARTHTIME Tracer Calibration Part I).
792 *Geochimica et Cosmochimica Acta* 164, 464-480 (2015).
- 793 70. McLean, N.M. , Condon D.J., Schoene, B. & Bowring, S.A. Evaluating uncertainties in
794 the calibration of isotopic reference materials and multi-element isotopic tracers

795 (EARTHTIME Tracer Calibration Part II). *Geochimica et Cosmochimica Acta* 164, 481-502
796 (2015).

797 71. Wolf, R. A., Farley, K. A. & Kass, D. M. Modeling of the temperature sensitivity of the
798 apatite (U–Th)/He thermochronometer. *Chemical Geology* 148, 105–114 (1998).

799 72. McDougall, I., & Harrison, T. M. *Geochronology and Thermochronology by the*
800 *⁴⁰Ar/³⁹Ar Method*. (Oxford University Press on Demand, 1999).

801 73. Cassata, W. S. & Renne, P. R. Systematic variations of argon diffusion in feldspars and
802 implications for thermochronometry. *Geochimica et Cosmochimica Acta* 112, 251–287
803 (2013).

804

805 **Acknowledgements**

806 This project was funded by BHP supporting the PhD of Marit van Zalinge. BHP have given
807 permission to publish. Zircon and sanidine analyses were supported by Natural Environment
808 Research Council Isotope Geosciences Facilities Steering Committee grant IP-1466-1114 and
809 Royal Society Research Grant RG140683 to FJC. Dan Condon is thanked for his help with the
810 analyses of inherited zircons. NERC are thanked for ongoing funding of the National
811 Environmental Isotope Facility. RSJS acknowledges support of a Leverhulme Trust Emeritus
812 Fellowship.

813

814 **Author contributions.**

815 Van Zalinge carried out field work, collected the samples and prepared them for
816 geochronological analyses. Mark conducted the ⁴⁰Ar/³⁹Ar analyses at the East Kilbride
817 laboratories. Keller and Mark applied a Bayesian model to interpret the geochronological
818 data. Mark and Sparks integrated and interpreted the geochronology and developed the

819 scientific narrative. Tremblay contributed argon diffusion modeling to estimate storage
820 temperatures and magma residence times for sanidine crystals. Rust analysed RT experiment
821 data for the diapir detachment timescale. Rust and Sparks developed the exchange flow
822 models for magma transport. Sparks and Mark led drafting the article and all authors
823 contributed to the writing. Cooper and Sparks supervised PhD student Van Zalinge.
824

Supplementary Files

This is a list of supplementary files associated with this preprint. Click to download.

- [TableED1.ArArdatasummary.xlsx](#)
- [TableED2.UPbLAICPMSdatasummary.xlsx](#)
- [SupplementaryMaterialsfigureandsampletable.pdf](#)